Accepted Manuscript

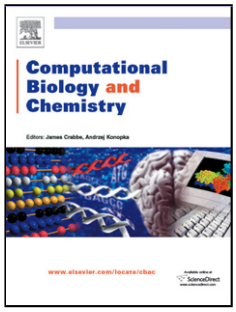

Title: A Ternary Complex Model of Sirtuin4-NAD^+-Glutamate Dehydrogenase

Authors: Yusuke Kato, Hiroshi Kihara, Kiyoshi Fukui, Masaki Kojima

PII: S1476-9271(16)30668-5
DOI: https://doi.org/10.1016/j.compbiolchem.2018.03.006
Reference: CBAC 6811

To appear in: *Computational Biology and Chemistry*

Received date: 16-12-2016
Revised date: 9-11-2017
Accepted date: 8-3-2018

Please cite this article as: Kato, Yusuke, Kihara, Hiroshi, Fukui, Kiyoshi, Kojima, Masaki, A Ternary Complex Model of Sirtuin4-NAD+-Glutamate Dehydrogenase.Computational Biology and Chemistry https://doi.org/10.1016/j.compbiolchem.2018.03.006

The published version is available via https://doi.org/10.1016/j.compbiolchem.2018.03.006

A Ternary Complex Model of Sirtuin4-NAD$^+$-Glutamate Dehydrogenase

Authors

Yusuke Kato[1,2,3,*], Hiroshi Kihara[2], Kiyoshi Fukui[3], Masaki Kojima[1]

Affiliations

[1] School of Life Sciences, Tokyo University of Pharmacy and Life Sciences, 1432-1 Horinouchi, Hachioji 192-0392, Japan.

[2] Himeji Hinomoto College, 890 Koro, Himeji 679-2151, Japan.

[3] Institute for Enzyme Research, Tokushima University, 3-18-15 Kuramoto, Tokushima 770-8503, Japan

*Corresponding author should be addressed:

Institute for Enzyme Research, Tokushima University, 3-18-15 Kuramoto, Tokushima 770-8503, Japan; Tel. +81-88-633-7430; Fax. +81-88-633-7431; E-mail ysk.kt@tokushima-u.ac.jp

Graphical Abstract

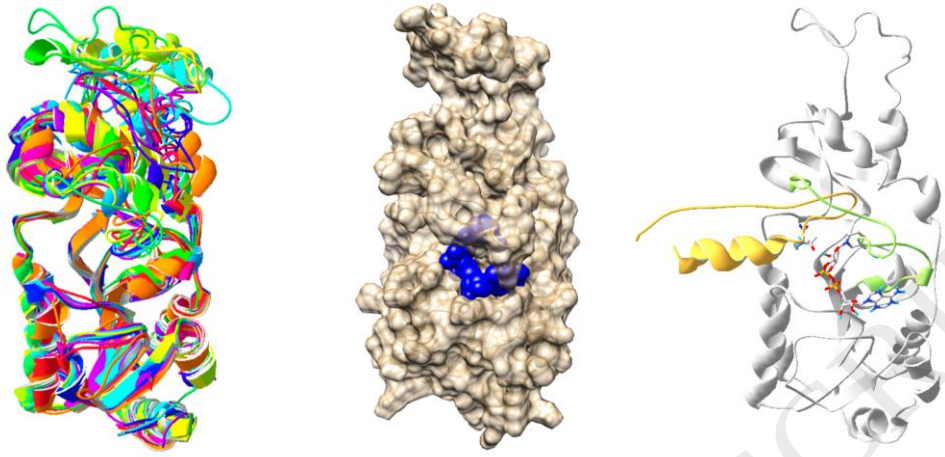

Highlights

- Homology models of Sitruin4 were built and evaluated.
- A Sirtuin4 model complexed with NAD^+ and glutamate dehydrogenase was built.
- Acetylated Lys171 of glutamate dehydrogenase and NAD^+ were close to each other.
- These suggest the mechanism of ADP-ribosylation of glutamate dehydrogenase.

Abstract

Sirtuin4 (Sirt4) is one of the mammalian homologues of Silent information regulator 2 (Sir2), which promotes the longevity of yeast, *C. elegans*, fruit flies and mice. Sirt4 is localized in the mitochondria, where it contributes to preventing the development of cancers and ischemic heart disease through regulating energy metabolism. The ADP-ribosylation of glutamate dehydrogenase (GDH), which is catalyzed by Sirt4,

downregulates the TCA cycle. However, this reaction mechanism is obscure, because the structure of Sirt4 is unknown. We here constructed structural models of Sirt4 by homology modeling and threading, and docked nicotinamide adenine dinucleotide$^+$ (NAD^+) to Sirt4. In addition, a partial GDH structure was docked to the Sirt4-NAD^+ complex model. In the ternary complex model of Sirt4-NAD^+-GDH, the acetylated lysine 171 of GDH is located close to NAD^+. This suggests a possible mechanism underlying the ADP-ribosylation at cysteine 172, which may occur through a transient intermediate with ADP-ribosylation at the acetylated lysine 171. These results may be useful in designing drugs for the treatment of cancers and ischemic heart disease.

Abbreviations

GDH Glutamate dehydrogenase

GDH 158–187 Residues 158–187 of human GDH

NAD Nicotinamide adenine dinucleotide

RMSD Root-mean-square deviation

RMSF Root-mean-square fluctuation

Sir2 Silent information regulator 2

Sirt Sirtuin

Keywords

Sirtuin; Metabolism; Homology modeling; Cancer; Docking; Ischemic heart disease

1. Introduction

Silent information regulator 2 (Sir2) genes have been shown to expand the lifespans of yeast, *C. elegans*, fruit flies, and mice [1-4]. Sirtuin4 (Sirt4) is one of seven mammalian gene products of Sir2 homologues. Many of the Sir2 family enzymes display nicotinamide adenine dinucleotide$^+$ (NAD^+)-dependent deacetylase activity. Sirt4 was previously reported to lack deacetylase activity [5]; however, recent studies have indicated the possibility of deacetylase and delipoylase activities [6-9]. In addition, Sirt4 catalyzes the ADP-ribosylation of glutamate dehydrogenase (GDH) with NAD^+ as a substrate [5]. The activity of GDH is inhibited by ADP-ribosylation of the C172 residue at the active site of GDH [5, 10]. Sirt4 is localized at the mitochondria, where it regulates the energy metabolic pathways, such as the TCA cycle and the oxidation of fatty acids by downregulating the activities of GDH and malonyl CoA decarboxylase, respectively [5, 7]. The upregulation of Sirt4 reduces transformation and

tumor development by downregulating GDH and, in turn, the TCA cycle [11]. In contrast, the TCA cycle is activated in cancer cells, because the expression of Sirt4 is suppressed by the mammalian target of rapamycin complex 1, mTORC1. Furthermore, Sirt4 is likely to play a crucial role in preventing cardiomyocyte loss during ischemic heart injury presumably through the regulatory mechanisms of energy metabolism [12].

The mechanism for the ADP-ribosylation of GDH by Sirt4 remains obscure because the structure of Sirt4 has been unknown. Because the mechanism by which Sirt4 regulates GDH is unclear, there has been a delay in drug design studies that target Sirt4 to treat cancer and ischemic heart disease. Recent progress in the field of prediction of protein structure and ligand binding modes has been remarkable [13, 14][15]. In the present study, we aimed to construct a structural model of a complex of human Sirt4 and GDH in order to elucidate the molecular mechanism underlying the ADP-ribosylation of GDH by Sirt4.

2. Materials and Methods

2.1. The modeling of the Sirt4-NAD^+ complex

We aligned Sir2 homologues with clustal W to determine the modeling region in the human Sirt4 sequence. Based on the alignment results, the homology modeling of human

Sirt4 was carried out with the sequence covering residue 40–314 using SWISS-MODEL [16] and Robetta [17]. I-TASSER, which ranked top in the recent Critical Assessment of Techniques for Protein Structure Prediction (CASP) contests, was used for threading [18]. The structural refinement of the models was performed by energy minimization using Swiss PDB Viewer with a partial implementation of the GROMOS96 force field [16]. The Sirt4 models were evaluated by PROCHECK [19], Verify3D [20], ERRAT [21] and energy calculation. The energy calculation was performed using Swiss PDB Viewer and the score function provided by the Rosetta suite [22]. The ENCoM server, which is used in the normal-mode analysis of coarse-grained models, was used to predict global structural changes [23]. A coarse-grained normal-mode analysis is suitable for predicting the large structural changes of proteins with relatively low CPU requirements. NAD^+ was docked with AutoDock Vina [24]. The scoring function of AutoDock Vina is based on “machine learning” rather than the physics-based energy potential. The accuracy of the prediction using a training set was ~80% based on an RMSD cutoff of 2 Å. The coordinates of NAD^+ were extracted from a PDB file of a Sir2 homologue complexed with NAD^+ (PDB code: 1ICI). The structures of the Sirt4 models and NAD^+ were prepared with the addition of gasteiger charges and polar hydrogens using AutoDockTools [25]. Unless otherwise mentioned, the illustrations of the protein

structures were produced with Swiss PDB viewer.

2.2. Docking of the GDH fragment

We predicted sites that showed a high propensity for binding on the surface of a Sirt4 model by STP [26]. Prediction by STP is based on the amino acid triplet types on the protein surface. STP predicts the top three binding sites on a protein with 88% accuracy.

The crystal structure of human GDH (PDB code: 1L1F) was downloaded from Protein Data Bank [27]. The coordinates of residues 158–187 of human GDH (GDH 158–187) were extracted from the PDB file for docking. Rigid body docking was carried out with the ZDOCK server [28] using a Sirt4 model and the coordinates of GDH 158–187. ZDOCK can predict the binding modes of protein-protein interaction with no experimental constraints. The scoring function of the ZDOCK server scores the shape complementarity, electrostatic charge, and interface atomic contact energy potential [29]. To allow for complete automation, no constraint was set for the docking simulation of GDH 158–187. The top 5 output models were observed in the docking trial. To confirm the ZDOCK result, rigid body docking was carried out using ClusPro without constraints. In the recent Critical Assessment of Prediction of Interactions (CAPRI) for protein-protein docking, ClusPro was shown to have the best record

among the automated servers [30].

Docking with the flexible GDH fragments was performed with FlexPepDock using the top 2 model of ZDOCK as a template [31]. FlexPepDock takes advantage of the framework of the Rosetta *ab initio* modeling suite to predict protein-peptide docking modes, and produces highly accurate models with an RMSD cutoff of 2 Å in more than 90% of the test sequences. The docking of the GDH fragments acetylated at lysine 171 was performed using AutoDock Vina.

2.3. The molecular dynamics simulations

After docking with AutoDock Vina, the complex model of Sirt4-NAD^+-GDH 158–187 was subjected to molecular dynamics (MD) simulations. The Amber ff14SB force field was applied to the complex [32]. The protein complex was placed in a periodic TIP3P box with the LEaP module of AMBER 14 [33]. The system was neutralized by replacing several TIP3P molecules with Cl^- ions. A 10-Å cut-off was applied to the non-bonded interactions according to the Lennard–Jones potential. Steepest descent minimization was performed followed by conjugate gradient minimization with the Particle Mesh Ewald method with constant-volume periodic boundaries and with position restraints for the protein atoms. A 200-ps heating

procedure was performed from 0 to 300 K under constant volume periodic boundaries. Equilibration and production MD were carried out for 10 ns with a constant pressure periodic boundary at 1 atm and 300 K without position restraints. The MD simulations for acetylated GDH 158–187 were performed under the same conditions.

2.4. Calculation of the binding free energy of NAD^+

The binding free energy (ΔG_{bind}) of the interaction between NAD^+ and the Sirt4 model was calculated based on the molecular mechanics energies combined with the generalized Born and surface area (MM/GBSA) method implemented in the AmberTools14 suite [34] [35]. The energy components including the molecular mechanical energy (ΔE^{MM}) and solvation energy (ΔG^{solv}) were defined as below [36]. The entropy term ($T\Delta S^{MM}$) was calculated based on the quasi-harmonic approximation [37].

$$\Delta G_{bind} = \Delta G^{MM} + \Delta G^{solv} = \Delta H_{bind} - T\Delta S^{MM}$$

$$\Delta G^{MM} = \Delta E^{MM} - T\Delta S^{MM}$$

$$\Delta H_{bind} = \Delta E^{MM} + \Delta G^{solv}$$

$$\Delta E^{MM} = \Delta E_{vdw} + \Delta E_{elec}$$

$$\Delta G^{solv} = \Delta G^{solv}_{polar} + \Delta G^{solv}_{nonpolar}$$

3. Results

3.1. Building the Sirt4 model

We carried out the homology modeling of amino acid residues 40–314 of human Sirt4 using SWISS-MODEL and Robetta (**Fig 1**). Homology modeling accurately predicts protein structures when there is more than ~30% identity between a target sequence and template structures [38]. It becomes difficult to align a target sequence with the sequence of a template structure when the identity is less than 30%, as this leads to significant errors in the model structure. **Table 1** shows the identities and coverage between the Sirt4 sequence and the template structures that were used in the homology modeling. All of the templates in **Table 1** had >30% identity but did not have 100% coverage; thus the applicability of homology modeling to Sirt4 is borderline.

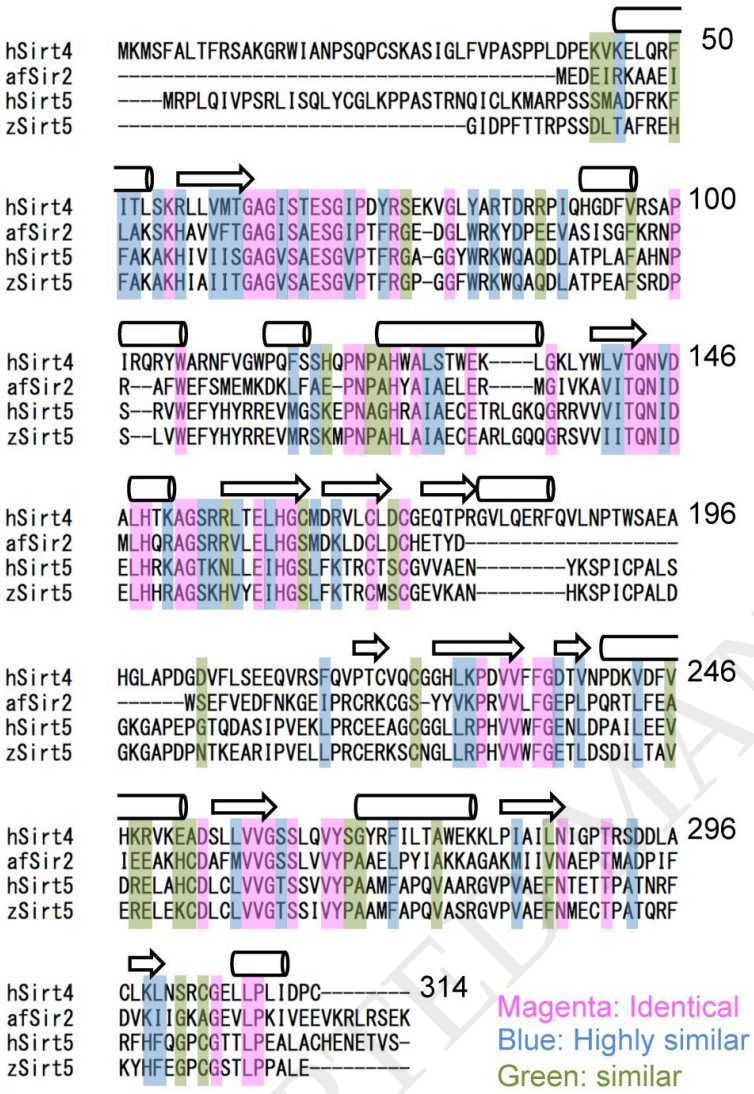

Fig 1. The alignment of the Sir2 homologues

hSirt4, afSir2, hSirt5 and zSirt5 stand for human Sirt4, *Archaeoglobus fulgidus* Sir2, human Sirt5 and zebrafish Sirt5, respectively. The residue numbers of human Sirt4 are shown. The locations of α-helices (cylinders) and β-strands (arrows) of the Sirt4 model are shown above the sequences.

In contrast, threading can be applied to model sequences that show much lower identity to templates. Thus, in addition to homology modeling, we carried out threading using I-TASSER, which can construct accurate structural models with low sequence identities to templates [39, 40]. I-TASSER uses multiple scoring profiles for a target sequence and multiple structural templates from Protein Data Bank, and then constructs a model by assembling the template fragments.

SWISS-MODEL, Robetta and I-TASSER each produced multiple models, which appeared similar to each other (**Fig 2A**). The superposition of all of the models showed that they had a common global fold (**Fig 2B**), which suggests the accuracy of the fold.

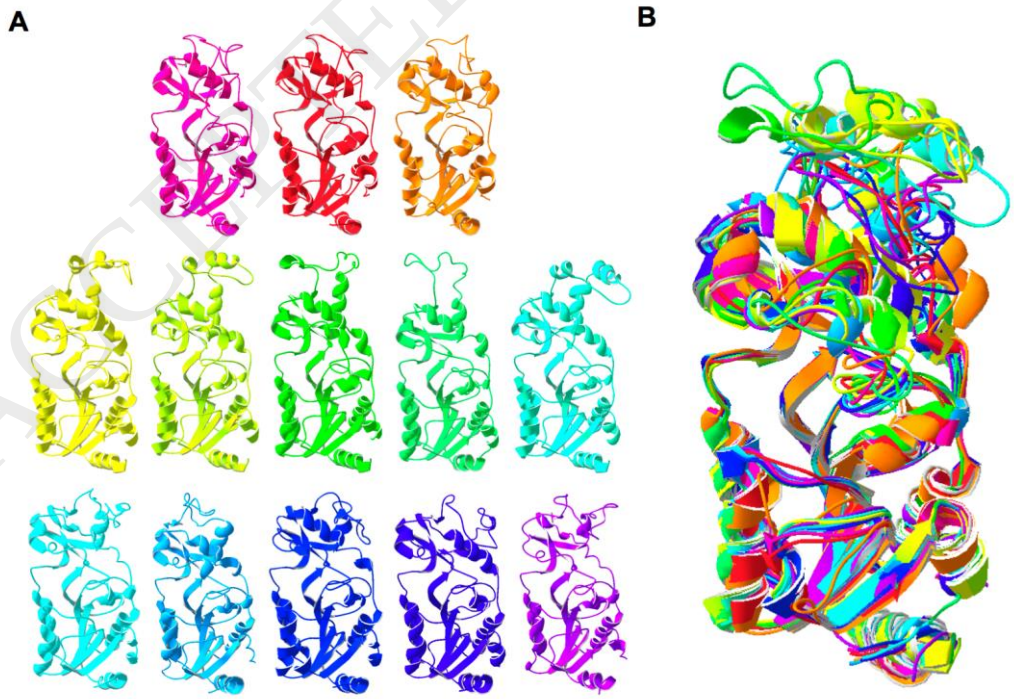

Fig 2. The model structures of Sirt4

(A) The models constructed in the present study are shown for comparison. The models in the top, middle and bottom rows were constructed by SWISS-MODEL, Robetta, and I-TASSER, respectively.

(B) All the models shown in (A) are superposed.

To select the most appropriate models, we evaluated the models in terms of PROCHECK, Verify3D, ERRAT and energy calculation. The models from Robetta showed no disallowed residues in the Ramachandran plots produced by PROCHECK, whereas the other models showed several disallowed residues (**Table 2**). The Robetta models showed larger numbers of favored residues than the other models. Verify3D and ERRAT also suggested high quality of the Robetta models (**Tables 3 and 4**). In addition, energy calculation by two different methods revealed that the Robetta models showed the lowest values (**Table 5**). A coarse-grained normal-mode analysis was performed to confirm the structural stability. The results predicted that the overall fold of the Robetta model was maintained while dynamic structural changes were observed (**Fig 3**). Accordingly, the Robetta models were used in the subsequent NAD^+-docking.

Fig 3. The dynamic structural motion of Sirt4 model

This illustration is based on the results from the coarse-grained normal-mode analysis with the ENCoM server.

3.2. The Docking of NAD^+

Sirt4 uses NAD^+ as a substrate for ADP-ribosylation (**Figs. 4A and B**). We therefore examined the docking of NAD^+ to the Robetta models using AutoDock Vina. The docking results indicated that NAD^+ docked with the interior grooves of the 4th Robetta model with a pose that was similar to those observed in the structures of the other Sir2 proteins (**Fig 4C**). In contrast, NAD^+ docked with different grooves in the other Robetta models. This suggests that only the 4th model possessed a similar groove structure to the other Sir2 proteins; however, the docking poses of NAD^+ with the 4th model still showed minor variation (**Fig 4D**). While the docked NAD^+ poses showed variation in the locations of the nicotinamide and adenine residues, one of the poses showed high similarity to that of NAD^+ in a crystal structure of human Sirt5 [41, 42]. The calculated energy value of this docking pose was lower than that of

the other poses, suggesting that this is the most plausible possibility. Nicotinamid (NCA) is an inhibitor against Sirt4 and docked with the interior groove of the 4th model with a similar pose to the NCA group of NAD^+ (**Fig. 4E**). This also supported the validity of the structure of the 4th model.

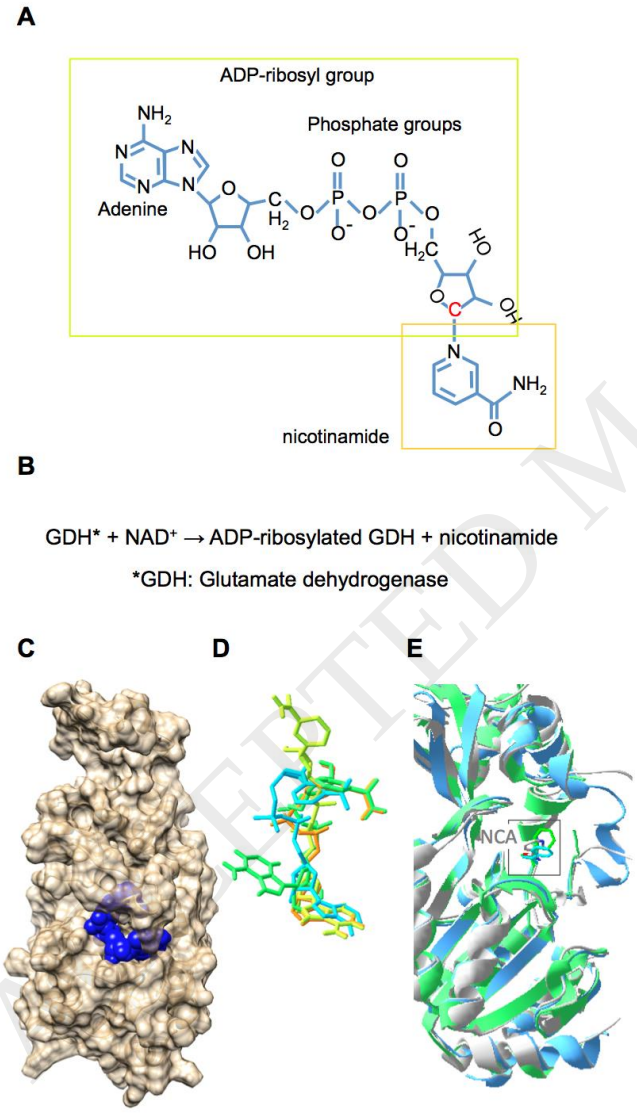

Fig 4. A model of the Sirt4-NAD^+ complex

(A) The structural formula of NAD^+. Reactive C1' is colored red.

(B) The chemical equation of the reaction catalyzed by Sirt4.

(C) The surface representation of a complex model of Sirt4-NAD^+. The surface of the Sirt4 model is transparent, whereas NAD^+ is shown as a blue nontransparent object. This panel was made with UCSF Chimera [43].

(D) Configurations of NAD^+ docked to Sirt4 as well as that of NAD^+ in complex with human Sirt5 (cyan, PDB code: 4G1C) are superposed. The configuration that docked best with Sirt4, which is also shown in (C), is colored orange.

(E) Docking with NCA. Ribbon models of afSir2 (PDB code: 1YC2), Sir2 from *Thermotoga maritima* (PDB code: 1YC5) and the 4th Robetta model of Sirt4 are colored sky blue, green and gray, respectively. NCA docked with the 4th model was depicted in CPK coloring, whereas NCAs from 1YC2 and 1YC5 are colored sky blue and green, respectively.

3.3. The docking of the GDH fragment

It has been suggested that Sirt4 ADP-ribosylates C172 at the active site of GDH using NAD^+ [5, 10]. In the proposed mechanism of ADP-ribosylation by Sir2 proteins from microorganisms, an acetylated lysine residue of a substrate protein is first ADP-ribosylated to form a reaction intermediate, followed by the translocation of the ADP-ribosyl group to the final site of ADP-ribosylation [44, 45].

It should be noted that the acetyl lysine and the final ADP-ribosylation site should be accessible to each other for the translocation. Similarly to other mitochondrial proteins, multiple lysine residues of GDH are acetylated [42, 46, 47]. Among these, K171 is the closest acetylation site to C172 (**Fig 5A**). Thus, K171 of GDH is likely to play an important role in the ADP-ribosylation at C172. This is compatible with the finding that the glutamate residue next to acetylated Lys15 is ADP-ribosylated in histone H1.1, which is a possible substrate of Sirtuins [48] (http://www.uniprot.org/uniprot/Q02539).

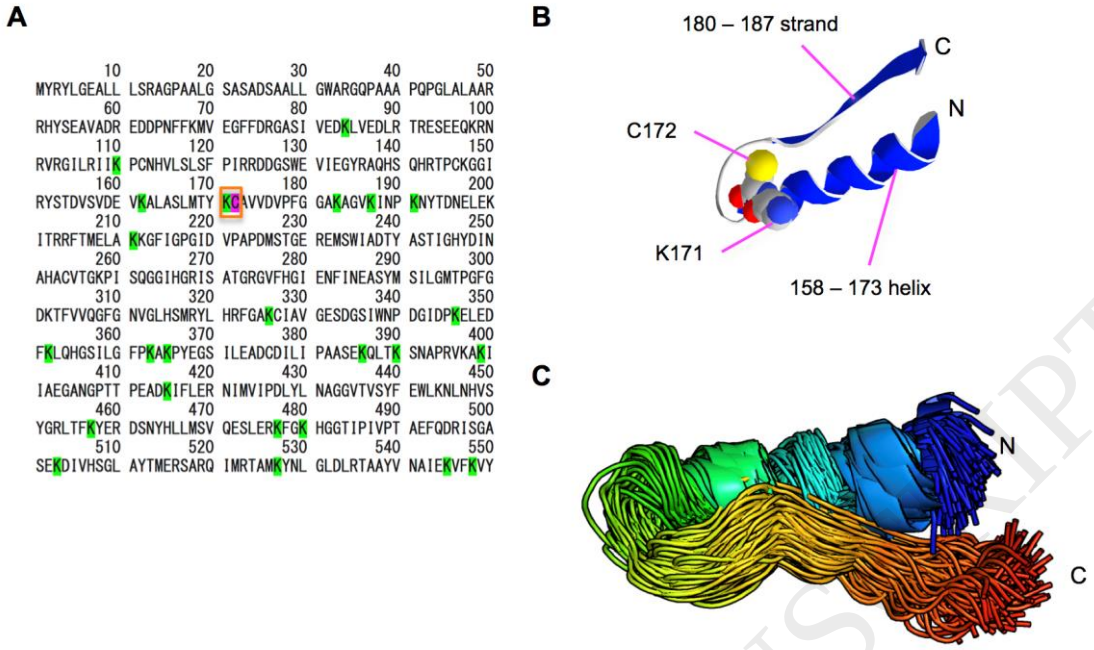

Fig 5. The sequence and structure of GDH

(A) The full length of the human GDH sequence. Green and magenta shading indicates the sites of acetylation and ADP-ribosylation, respectively. The orange box indicates K171 and C172.

(B) The region of 158–187 of GDH, GDH 158–187, forming a helix-loop-strand configuration.

(C) The dynamic structural motion of GDH 158 - 187 was simulated with a coarse-grained normal-mode analysis.

Fig 5B shows relative locations of K171 and C172 in the crystal structure of GDH [49]. These residues are located at an edge of the 158–173 helix, followed by the bending 174–179 loop and the extended 180–187 strand. We call this region GDH 158–187. To predict the structural change of GDH 158–187, we performed a coarse-grained normal-mode analysis with the ENCoM server [23], and found no change of the global fold of GDH 158–187 (**Fig 5C**). This suggested that the structure of GDH 158–187 is maintained when it binds to Sirt4,

so that we used the GDH 158–187 coordinates for docking to the Sirt4 model.

Prior to the docking simulation, we investigated sites on the surface of the Sirt4 model that showed a high propensity for binding using STP, and found high propensity sites around the center of the model (circled in **Fig 6A**). Using the ZDOCK server, we then carried out automated rigid body docking between the Sirt4 model and the helix-loop-strand structure of GDH 158 –187. We found that GDH 158–187 was docked into a hole composed of the 63–91 loop of Sirt4, and that K171 of GDH was located close to NAD^+ (**Fig 6B**). This result is consistent with the STP result. Moreover, a rigid body docking simulation with ClusPro showed a similar docking pose to that obtained with ZDOCK (**Fig 6C**).

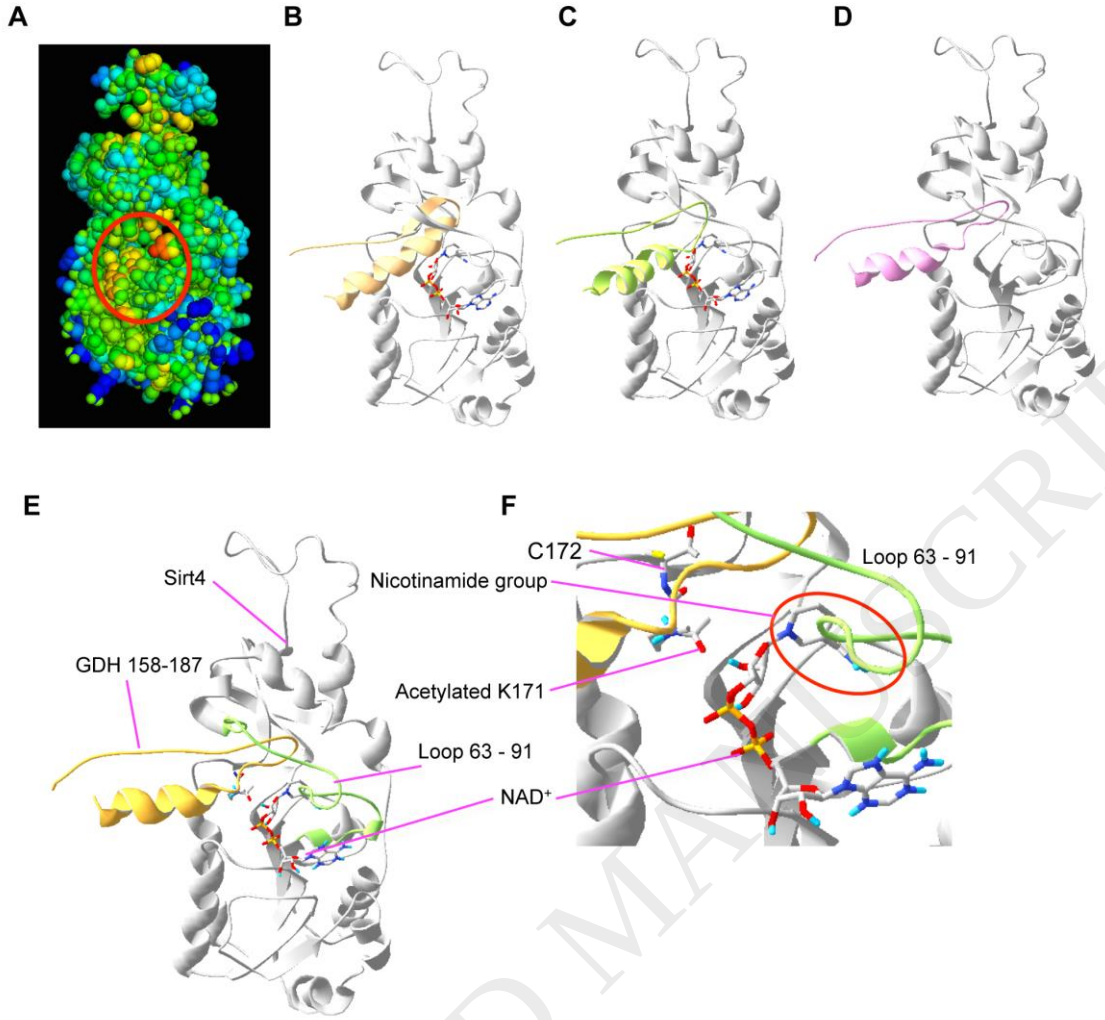

Fig 6. Docking GDH to Sirt4

(A) The prediction of the propensity of the binding sites mapped on the Sirt4 model. The hot and cold colors indicate high and low propensity sites, respectively. A cluster of high propensity sites is circled. This panel was made with PyMol (Schrödinger, LLC., New York, NY).

(B) The results of rigid body docking using ZDOCK. GDH 158–187 was docked to the Sirt4 model. GDH 158–187 and Sirt4 are depicted as yellow and light gray ribbons, respectively. NAD^+ is depicted as a stick model. The illustration shows the second-ranked model in the docking simulation. The top-ranked model of GDH 158–187 docking was unrealistic, because the N- and C-termini were buried in Sirt4. We note that GDH 158–187 is a part of GDH; thus, in reality, the N- and C-termini are connected to the rest of the GDH sequence. The illustrated model has exposed N- and C-termini, which is necessary for connection to the rest of the GDH sequence.

(C) The results of rigid body docking using ClusPro. The illustration shows the top-ranked model. The docking conditions were the same as those shown in (B). GDH is colored green.

(D) The results of flexible docking. The structure of GDH 158–187 (magenta) was flexibly perturbed and docked to the Sirt4 model.

(E) The results of the docking of the acetylated GDH fragment. GDH 158–187 (yellow) with acetylated K171 was docked to Sirt4. The 63–91 loop of Sirt4 is indicated in green.

(F) A magnified view of (E)

To obtain a refined docking pose, we carried out flexible docking with FlexPepDock in which the structure of GDH 158–187 was flexibly perturbed by the conformational sampling protocols that are implemented in the Rosetta suite. A docking solution indicated a pose in which the GDH model with an altered structure was docked into the hole composed of the 63–91 loop, while the overall structure of the GDH fragment was similar to that of the crystal structure (**Fig 6D**).

FlexPepDock does not take the modifications of amino acids and cofactors into account. We therefore examined the docking of acetylated GDH 158–187 to the complex of Sirt4-NAD^+ using AutoDock Vina. The results showed that acetylated GDH 158–187 in the helix-loop-strand conformation was docked to Sirt4 with NAD^+ in a similar pose to that which was output by FlexPepDock (**Figs 6E and F**). We evaluated the docking model and found that the results from PROCHECK, Verify3D, ERRAT and the energy calculations indicated no problems with regard to the quality of the model (**Table 6**). As mentioned above, the 63–91

loop fringed the docked GDH 158 - 187 model in the ternary complex model (**Fig. 6E)**. This loop was detached from the main fold of Sirt4, forming a hole. Such a hole is also present on the surface of afSir2 [50].

3.4. Dynamic properties of the Sirt4-NAD^+-GDH model

In order to examine the extent of the structural stability of the Sirt4-NAD^+-GDH model, an MD simulation was performed. The RMSD of the complex model tended to converge after 4 ns. This suggested that the complex structure of the model was stable and that it had reached an equilibrium, supporting the validity of the complex model (**Fig. 7A**). The RMSD between the initial and final trajectories of the main fold of Sirt4 was ~2.8Å, which suggested the stability of the global fold of the Sirt4 model. (**Fig 7B)**. The root-mean-square fluctuation (RMSF) was calculated to evaluate the dynamic properties of the complex. Residues 77–80, 190–210 and 221–224 of Sirt4 and the N- and C- termini of acetylated GDH 158–187 were flexible (**Fig. 7C, D**). The flexible regions were mapped on the Sirt4 model structure (**Fig. 7E**). Residues 190–210 formed a long loop structure at the top of the model. Residues 77 –80 belonged to the 63–91 loop.

After the 50ns MD simulation, the small domain of Sirt4 and GDH 158-187 together

rotated clockwise relative to the Rossmann domain of Sirt4 (**Fig. 7B**) and many hydrogen bonds formed or strengthened between NAD^+ and the Rossmann domain (**Table 7, Fig. 7F**). The formation of the hydrogen bonds was accompanied by the conformational change in the Rossman domain and NAD^+. The 261-267 loop moved toward NAD^+ by the shortening of the hydrogen bond between S262 and the phosphate group of NAD^+ (**Fig. 7B, F**). As a consequence, GDH 158 – 187 was pushed away and the structure of the 92 – 96 helix and the 63 – 91 loop changed.

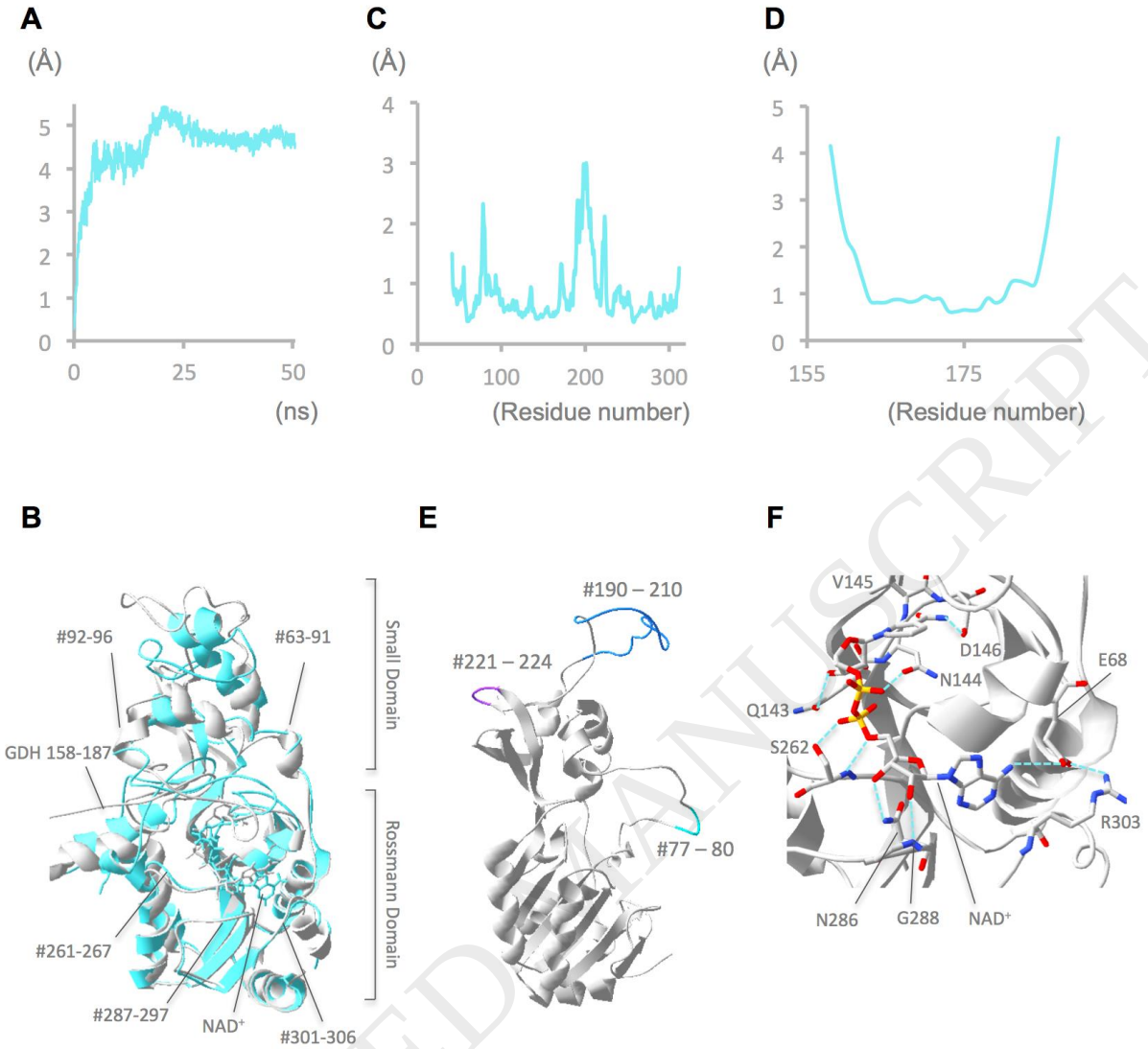

Fig 7. Dynamic properties the Sirt4-NAD$^+$- GDH 158–187 model

(A) The RMSD values of the backbone Cα atoms in the course of the MD simulation of the Sirt4-NAD$^+$-GDH 158–187 model.

(B) Comparison of the structures before (gray) and after (cyan) the MD simulation.

(C) The RMSF of Sirt4 in complex with NAD$^+$ and GDH 158–187. The RMSD values of individual residues, which were calculated from the trajectories of the MD simulations after 5 ns, are plotted.

(D) The RMSF of GDH 158–187 in the complex.

(E) The mapping of the flexible regions on the Sirt4 model. The amino acid residue numbers of the colored regions are indicated.

(F) An enlarged view of the ternary complex model after the MD simulation. NAD$^+$ and the residues that formed hydrogen bonds with NAD$^+$ are depicted as stick models. Hydrogen bonds between NAD$^+$ and Sirt4 are depicted as dotted lines in cyan.

It is natural to question how C172 is ADP-ribosylated. In the ADP-ribosylation mechanism proposed for Sir2 proteins from microorganisms, ADP-ribosylation is mediated through the formation of a transient intermediate with acetylated lysine ADP-ribosylated [44, 45]. Accordingly, we hypothesize that ADP-ribosylation at C172 occurs through the formation of an intermediate in which acetylated K171 is transiently ADP-ribosylated. At 3.75 Å, the oxygen atom of the acetyl group on K171 and the C1' atom of NAD^+ in the ternary complex model were in close proximity to each other (within the approximate van der Waals contact distance) (**Fig 8A**). The minimum, average and maximum distances between these atoms in the MD trajectories were 2.83, 3.48 and 5.21 Å, respectively (**Fig. 8B**). Thus, it is possible that this acetyl group may be ADP-ribosylated. In addition, the acetyl group on K171 and the final ADP-ribosylation site, the thiol group of C172, are able to become close enough to each other to allow the translocation of the ADP-ribosyl group, given flexible conformational changes of the side chains of K171 and C172 (**Fig 8C**). To support this hypothesis, the distance between the sulfur atom of C172 and the oxygen atom of acetylated K171 was measured in the trajectories of the MD simulation of GDH 158–187. The distance showed extensive fluctuation, with minimum and maximum values of 2.98 and 12.8 Å, respectively,

and frequently became shorter than 4.0 Å (within the approximate van der Waals contact distance) (**Fig. 8D**). Taken together these findings suggested a possible mechanism for the final ADP-ribosylation at C172 through the intermediate with ADP-ribosylation at acetylated K171.

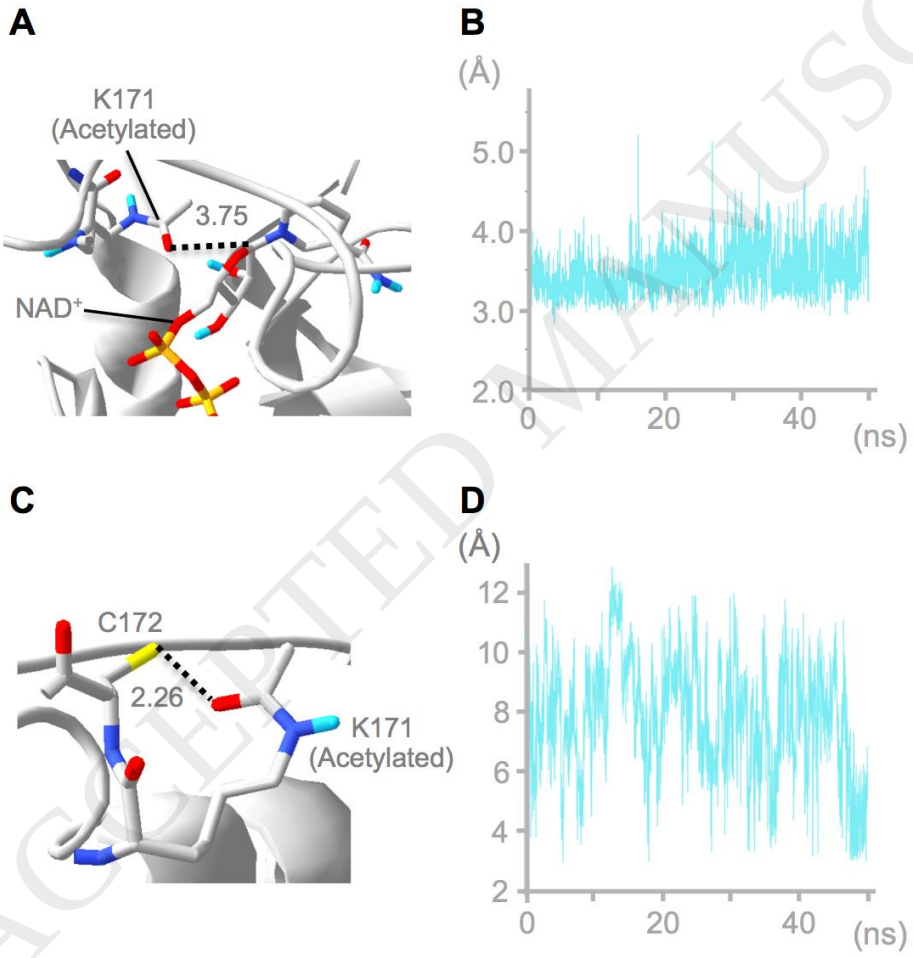

Fig 8. The distance between reactive atoms

(A) The distance (Å) between the oxygen atom of the acetyl group on K171 and C1' atom of NAD^+ in the model is shown as a dotted line.

(B) The fluctuation of the distance between the oxygen atom of acetylated K171 and C1' atom in the course of the MD simulation.

(C) The possible distance (Å) between the oxygen atom of acetylated K171 and the thiol sulfur of C172. This conformation was produced by manual conformational changes of the side chains of acetylated K171 and C172 using Swiss PDB Viewer.

(D) Fluctuation of the distance between the oxygen atom of acetylated K171 and the thiol sulfur of C172 in the trajectories of GDH 158–187.

4. Discussion

Sirt4, which is localized to the mitochondria, regulates the TCA cycle and fatty acid oxidation [5, 7], and plays important roles in the suppression of cancers and ischemic heart disease [11, 12]. Sirt4 contributes to many of these biological events through its ADP-ribosylation activity to GDH using NAD^+ as a substrate to downregulate GDH. GDH catalyzes the oxidative deamination of glutamate to produce α-ketoglutaric acid, which is an intermediate in the TCA cycle. We aimed to build structural models of human Sirt4 in complex with NAD^+ and GDH 158–187 in order to elucidate the detailed mechanism by which Sirt4 regulates the metabolism. The Sirt4 models were first built by homology modeling and threading, and showed a common global fold. Subsequently, we docked NAD^+ to the models that were energetically stable to build a complex model with NAD^+. The docking pose of NAD^+ in the Sirt4-NAD^+ complex model was similar to that in a crystal structure of the Sirt5-NAD^+ complex [41, 42]. This suggested that the docking model

possesses a similar structure of internal grooves to Sirt5. A normal mode analysis showed that the helix-loop-strand structure of GDH 158–187 was maintained, which suggested that this fold is maintained when GDH binds Sirt4. Thus, we docked the structure of GDH 158-187 to the Sirt4 model and found a common docking pose among the Sirt4-NAD^+-GDH 158–187 complex models that were predicted by multiple methods. An analysis of the MD trajectories indicated that the Sirt4-NAD^+-GDH 158–187 complex model converged towards a more stable structure, maintaining the global fold of the initial structure. NCA and sirtinol are known inhibitors of Sirt4 [5]. NCA docked with the groove with which the NCA group of NAD^+ docked. In addition, the pose of NCA docked with the Sirt4 model was quite similar to those in the crystal structures of the Sir2 protein-NCA complexes (**Fig 4E**) [51]. Taken together, these findings supported the validity of the model structure.

The number of hydrogen bonds between NAD^+ and Sirt4 in the ternary complex model increased after the model reached an equilibrium in the MD simulation. The corresponding hydrogen bonds are formed in the crystal structures of the complexes of NAD^+ and the Sir2/Sirtuin proteins including afSir2 and hSirt5 [42, 50]. The increase in the number of the hydrogen bonds was followed by changes in the structures of loops in the Rossmann domain including the 261 – 267 loop. Similar structural differences of the corresponding loops are

observed between the apo and NAD^+-bound forms of afSir2. We also observed a rotation of the small domain relative to the Rossmann domain in the MD simulation. It has been reported that the small domain rotates relative to the Rossmann domain in several Sir2/Sirtuin proteins including afSir2 and Sirt5 [50, 52].

While the K_D and K_m values for NAD^+ bound to Sirt4 have been unknown, the K_m values for NAD^+ bound to the other Sirtuins are approximately in the range of 10^{-4} – 10^{-6} M, which corresponds to -5 – -8 kcal/mol of the binding free energy [53]. The binding free energy (ΔG_{bind}) of the interaction between Sirt4 and NAD^+ was calculated according to the MM/GBSA method and found to be similar to those of the interactions between the other Sirtuins and NAD^+ (**Table 8**). ΔE_{elec} was relatively large, which was in line with the large number of the hydrogen bonds between Sirt4 and NAD^+ observed after the MD simulation.

A further trajectory analysis suggested that the distances between acetylated K171 and NAD^+ and between acetylated K171 and C172 could become short enough to allow them to react with each other. These results are compatible with a possible reaction mechanism in which the ADP-ribosylation of C172 occurs through an intermediate with the

ADP-ribosylation of K171. This possibility is in line with the proposed mechanism that ADP-ribosylation by Sir2 proteins is mediated through an intermediate with the ADP-ribosylation of acetylated lysine [44]. Furthermore, it was suggested that an acetylated lysine residue is required when the Sir2 protein ADP-ribosylates residues other than arginine [45]. Thus, ADP-ribosylation at C172 through an intermediate with the ADP-ribosylation of K171 is a possible scenario.

The regulations of the metabolism by Sirt4 have a great impact on ischemic heart injury, the DNA damage response program, and the development of cancer and the glial cells [11, 12, 54, 55]. Haigis et al. reported that Sirt4 downregulates the secretion of insulin from pancreatic β cells by inhibiting GDH in the mitochondria [5]. The inhibition of GDH by Sirt4 in cancer cells represses the glutamine metabolism, leading to the suppression of cancer cell activity [54]. In vitro knockdown of Sirt4 increases the activity of GDH and promotes the proliferation and migration of cells [56]. The expression level of Sirt4 in breast cancer is correlated with those of the estrogen receptor, progesterone receptor, nuclear-associated antigen Ki-67 and tumor protein p53 [57]. Sirt4 and GDH are together expressed in the brain and play important roles in brain development and ageing [55, 58, 59]. It has been suggested that SIRT4 is a key player in preventing hypoxia-induced cardiomyocyte apoptosis [12]. Thus,

it is anticipated that the development of drugs that activate Sirt4 will contribute to the suppression of cancer and the survival of cardiomuscular cells in patients with ischemic heart injury. Resveratrol is an activator of Sirt1 and 5 and its action on Sirt1 may increase the longevity of yeast, worms, flies and mice [1, 60, 61]. In contrast, it was reported that resveratrol inhibits Sirt3 [62]. To our knowledge, no compounds have ever been found to activate Sirt4, while inhibitors of Sirt4 have been reported as discussed above [5]. Because loss of Sirt4 increases the secretion of insulin in mice, inhibitors of Sirt4 may have the potential to be used as seed compounds for glycometabolism ameliorators. Recently, structure-based drug design based on homology models has successfully produced various compounds [63, 64]. Thus, we hope that the Sirt4-NAD^+-GDH 158–187 ternary complex model and the mechanism proposed in the present report will contribute to the development of the drugs that activate Sirt4 to treat cancer and ischemic heart injury.

Acknowledgements

This work was supported by The Vehicle Racing Commemorative Foundation and by Joint Usage and Joint Research Programs, the Institute of Advanced Medical Sciences, Tokushima University.

References

1. Blander G, Guarente L. The Sir2 family of protein deacetylases. Annual review of biochemistry. 2004;73:417-35. Epub 2004/06/11. doi: 10.1146/annurev.biochem.73.011303.073651. PubMed PMID: 15189148.

2. Kanfi Y, Naiman S, Amir G, Peshti V, Zinman G, Nahum L, et al. The sirtuin SIRT6 regulates lifespan in male mice. Nature. 2012;483(7388):218-21. Epub 2012/03/01. doi: 10.1038/nature10815. PubMed PMID: 22367546.

3. Mercken EM, Hu J, Krzysik-Walker S, Wei M, Li Y, McBurney MW, et al. SIRT1 but not its increased expression is essential for lifespan extension in caloric-restricted mice. Aging cell. 2014;13(1):193-6. Epub 2013/08/15. doi: 10.1111/acel.12151. PubMed PMID: 23941528; PubMed Central PMCID: PMCPMC3907112.

4. Satoh A, Brace CS, Rensing N, Cliften P, Wozniak DF, Herzog ED, et al. Sirt1 extends life span and delays aging in mice through the regulation of Nk2 homeobox 1 in the DMH and LH. Cell metabolism. 2013;18(3):416-30. Epub 2013/09/10. doi: 10.1016/j.cmet.2013.07.013. PubMed PMID: 24011076; PubMed Central PMCID: PMCPMC3794712.

5. Haigis MC, Mostoslavsky R, Haigis KM, Fahie K, Christodoulou DC, Murphy AJ, et al. SIRT4 inhibits glutamate dehydrogenase and opposes the effects of calorie restriction in pancreatic beta cells. Cell. 2006;126(5):941-54. Epub 2006/09/09. doi: 10.1016/j.cell.2006.06.057. PubMed PMID: 16959573.

6. Mathias RA, Greco TM, Oberstein A, Budayeva HG, Chakrabarti R, Rowland EA, et al. Sirtuin 4 is a lipoamidase regulating pyruvate dehydrogenase complex activity. Cell. 2014;159(7):1615-25. Epub 2014/12/20. doi: 10.1016/j.cell.2014.11.046. PubMed PMID: 25525879; PubMed Central PMCID: PMCPMC4344121.

7. Laurent G, German NJ, Saha AK, de Boer VC, Davies M, Koves TR, et al. SIRT4 coordinates the balance between lipid synthesis and catabolism by repressing malonyl CoA decarboxylase. Molecular cell. 2013;50(5):686-98. Epub 2013/06/12. doi: 10.1016/j.molcel.2013.05.012. PubMed PMID: 23746352; PubMed Central PMCID: PMCPmc3721068.

8. Rauh D, Fischer F, Gertz M, Lakshminarasimhan M, Bergbrede T, Aladini F, et al. An acetylome peptide microarray reveals specificities and deacetylation substrates for all human sirtuin isoforms. Nature communications. 2013;4:2327. Epub 2013/09/03. doi: 10.1038/ncomms3327. PubMed PMID: 23995836.

9. Feldman JL, Baeza J, Denu JM. Activation of the protein deacetylase SIRT6 by long-chain fatty acids and widespread deacylation by mammalian sirtuins. The Journal of biological chemistry. 2013;288(43):31350-6. Epub 2013/09/21. doi: 10.1074/jbc.C113.511261. PubMed PMID: 24052263; PubMed Central PMCID: PMCPmc3829447.

10. Choi MM, Huh JW, Yang SJ, Cho EH, Choi SY, Cho SW. Identification of ADP-ribosylation site in human glutamate dehydrogenase isozymes. FEBS letters. 2005;579(19):4125-30. Epub 2005/07/19. doi: 10.1016/j.febslet.2005.06.041. PubMed PMID: 16023112.

11. Csibi A, Fendt SM, Li C, Poulogiannis G, Choo AY, Chapski DJ, et al. The mTORC1 pathway stimulates glutamine metabolism and cell proliferation by repressing SIRT4. Cell. 2013;153(4):840-54. Epub 2013/05/15. doi: 10.1016/j.cell.2013.04.023. PubMed PMID: 23663782; PubMed Central PMCID: PMCPmc3684628.

12. Liu B, Che W, Xue J, Zheng C, Tang K, Zhang J, et al. SIRT4 prevents hypoxia-induced apoptosis in H9c2 cardiomyoblast cells. Cell Physiol Biochem. 2013;32(3):655-62. Epub 2013/09/14. doi: 10.1159/000354469. PubMed PMID: 24029877.

13. Dorn M, MB ES, Buriol LS, Lamb LC. Three-dimensional protein structure prediction: Methods and computational strategies. Computational biology and chemistry. 2014;53pb:251-76. Epub 2014/12/03. doi: 10.1016/j.compbiolchem.2014.10.001. PubMed PMID: 25462334.

14. Negami T, Shimizu K, Terada T. Coarse-Grained Molecular Dynamics Simulations of Protein-Ligand Binding. Journal of computational chemistry. 2014;35(25):1835-45. doi: 10.1002/jcc.23693. PubMed PMID: WOS:000340878000004.

15. Kim H, Kihara D. Protein structure prediction using residue- and fragment-environment potentials in CASP11. Proteins. 2016;84 Suppl 1:105-17. Epub 2015/09/08. doi: 10.1002/prot.24920. PubMed PMID: 26344195; PubMed Central PMCID: PMCPMC4781684.

16. Guex N, Peitsch MC. SWISS-MODEL and the Swiss-PdbViewer: an environment for comparative protein modeling. Electrophoresis. 1997;18(15):2714-23. Epub 1998/03/21. doi: 10.1002/elps.1150181505. PubMed PMID: 9504803.

17. Chivian D, Kim DE, Malmstrom L, Bradley P, Robertson T, Murphy P, et al. Automated prediction of CASP-5 structures using the Robetta server. Proteins. 2003;53 Suppl 6:524-33. Epub 2003/10/28. doi: 10.1002/prot.10529. PubMed PMID: 14579342.

18. Yang J, Yan R, Roy A, Xu D, Poisson J, Zhang Y. The I-TASSER Suite: protein structure and function prediction. Nature methods. 2015;12(1):7-8. Epub 2014/12/31. doi:

10.1038/nmeth.3213. PubMed PMID: 25549265; PubMed Central PMCID: PMCPmc4428668.

19. Laskowski RA, MacArthur MW, Moss DS, Thornton JM. PROCHECK: a program to check the stereochemical quality of protein structures. Journal of Applied Crystallography. 1993;26(2):283-91. doi: doi:10.1107/S0021889892009944.

20. Luthy R, Bowie JU, Eisenberg D. Assessment of protein models with three-dimensional profiles. Nature. 1992;356(6364):83-5. Epub 1992/03/05. doi: 10.1038/356083a0. PubMed PMID: 1538787.

21. Colovos C, Yeates TO. Verification of protein structures: patterns of nonbonded atomic interactions. Protein science : a publication of the Protein Society. 1993;2(9):1511-9. Epub 1993/09/01. doi: 10.1002/pro.5560020916. PubMed PMID: 8401235; PubMed Central PMCID: PMCPmc2142462.

22. Simons KT, Bonneau R, Ruczinski I, Baker D. Ab initio protein structure prediction of CASP III targets using ROSETTA. Proteins. 1999;Suppl 3:171-6. Epub 1999/10/20. PubMed PMID: 10526365.

23. Frappier V, Chartier M, Najmanovich RJ. ENCoM server: exploring protein conformational space and the effect of mutations on protein function and stability. Nucleic acids research. 2015;43(W1):W395-400. Epub 2015/04/18. doi: 10.1093/nar/gkv343. PubMed PMID: 25883149; PubMed Central PMCID: PMCPmc4489264.

24. Trott O, Olson AJ. AutoDock Vina: improving the speed and accuracy of docking with a new scoring function, efficient optimization, and multithreading. Journal of computational chemistry. 2010;31(2):455-61. Epub 2009/06/06. doi: 10.1002/jcc.21334. PubMed PMID: 19499576; PubMed Central PMCID: PMCPmc3041641.

25. Morris GM, Huey R, Lindstrom W, Sanner MF, Belew RK, Goodsell DS, et al. AutoDock4 and AutoDockTools4: Automated docking with selective receptor flexibility. Journal of computational chemistry. 2009;30(16):2785-91. Epub 2009/04/29. doi: 10.1002/jcc.21256. PubMed PMID: 19399780; PubMed Central PMCID: PMCPmc2760638.

26. Mehio W, Kemp GJ, Taylor P, Walkinshaw MD. Identification of protein binding surfaces using surface triplet propensities. Bioinformatics (Oxford, England). 2010;26(20):2549-55. Epub 2010/09/08. doi: 10.1093/bioinformatics/btq490. PubMed PMID: 20819959.

27. Berman HM, Westbrook J, Feng Z, Gilliland G, Bhat TN, Weissig H, et al. The Protein Data Bank. Nucleic acids research. 2000;28(1):235-42. Epub 1999/12/11. PubMed PMID: 10592235; PubMed Central PMCID: PMCPmc102472.

28. Pierce BG, Wiehe K, Hwang H, Kim BH, Vreven T, Weng Z. ZDOCK server: interactive docking prediction of protein-protein complexes and symmetric multimers. Bioinformatics (Oxford, England). 2014;30(12):1771-3. Epub 2014/02/18. doi: 10.1093/bioinformatics/btu097. PubMed PMID: 24532726; PubMed Central PMCID: PMCPmc4058926.

29. Pierce BG, Hourai Y, Weng Z. Accelerating protein docking in ZDOCK using an advanced 3D convolution library. PloS one. 2011;6(9):e24657. Epub 2011/09/29. doi: 10.1371/journal.pone.0024657. PubMed PMID: 21949741; PubMed Central PMCID: PMCPmc3176283.

30. Kozakov D, Beglov D, Bohnuud T, Mottarella SE, Xia B, Hall DR, et al. How good is automated protein docking? Proteins. 2013;81(12):2159-66. Epub 2013/09/03. doi: 10.1002/prot.24403. PubMed PMID: 23996272; PubMed Central PMCID: PMCPmc3934018.

31. London N, Raveh B, Cohen E, Fathi G, Schueler-Furman O. Rosetta FlexPepDock web server--high resolution modeling of peptide-protein interactions. Nucleic acids research. 2011;39(Web Server issue):W249-53. Epub 2011/05/31. doi: 10.1093/nar/gkr431. PubMed PMID: 21622962; PubMed Central PMCID: PMCPmc3125795.

32. Maier JA, Martinez C, Kasavajhala K, Wickstrom L, Hauser KE, Simmerling C. ff14SB: Improving the Accuracy of Protein Side Chain and Backbone Parameters from ff99SB. J Chem Theory Comput. 2015;11(8):3696-713. doi: 10.1021/acs.jctc.5b00255. PubMed PMID: WOS:000359500000019.

33. Case DA, Babin V, J.T. Berryman, R.M. Betz, Cai Q, Cerutti DS, et al. Amber 14. 2014.

34. Onufriev A, Bashford D, Case DA. Exploring protein native states and large-scale conformational changes with a modified generalized born model. Proteins. 2004;55(2):383-94. Epub 2004/03/30. doi: 10.1002/prot.20033. PubMed PMID: 15048829.

35. Miller BR, 3rd, McGee TD, Jr., Swails JM, Homeyer N, Gohlke H, Roitberg AE. MMPBSA.py: An Efficient Program for End-State Free Energy Calculations. J Chem Theory Comput. 2012;8(9):3314-21. Epub 2012/09/11. doi: 10.1021/ct300418h. PubMed PMID: 26605738.

36. Malaisree M, Rungrotmongkol T, Decha P, Intharathep P, Aruksakunwong O, Hannongbua S. Understanding of known drug-target interactions in the catalytic pocket of neuraminidase subtype N1. Proteins. 2008;71(4):1908-18. Epub 2008/01/05. doi: 10.1002/prot.21897. PubMed PMID: 18175324.

37. Schlitter J. Estimation of absolute and relative entropies of macromolecules using

the covariance matrix. Chemical Physics Letters. 1993;215(6):617-21. doi: https://doi.org/10.1016/0009-2614(93)89366-P.

38. Baker D, Sali A. Protein structure prediction and structural genomics. Science (New York, NY). 2001;294(5540):93-6. Epub 2001/10/06. doi: 10.1126/science.1065659. PubMed PMID: 11588250.

39. Xu D, Zhang J, Roy A, Zhang Y. Automated protein structure modeling in CASP9 by I-TASSER pipeline combined with QUARK-based ab initio folding and FG-MD-based structure refinement. Proteins. 2011;79 Suppl 10:147-60. Epub 2011/11/30. doi: 10.1002/prot.23111. PubMed PMID: 22069036; PubMed Central PMCID: PMCPmc3228277.

40. Zhang Y. I-TASSER: fully automated protein structure prediction in CASP8. Proteins. 2009;77 Suppl 9:100-13. Epub 2009/09/22. doi: 10.1002/prot.22588. PubMed PMID: 19768687; PubMed Central PMCID: PMCPmc2782770.

41. Szczepankiewicz BG, Dai H, Koppetsch KJ, Qian D, Jiang F, Mao C, et al. Synthesis of carba-NAD and the structures of its ternary complexes with SIRT3 and SIRT5. The Journal of organic chemistry. 2012;77(17):7319-29. Epub 2012/08/02. doi: 10.1021/jo301067e. PubMed PMID: 22849721.

42. Du J, Zhou Y, Su X, Yu JJ, Khan S, Jiang H, et al. Sirt5 is a NAD-dependent protein lysine demalonylase and desuccinylase. Science (New York, NY). 2011;334(6057):806-9. Epub 2011/11/15. doi: 10.1126/science.1207861. PubMed PMID: 22076378; PubMed Central PMCID: PMCPmc3217313.

43. Pettersen EF, Goddard TD, Huang CC, Couch GS, Greenblatt DM, Meng EC, et al. UCSF Chimera--a visualization system for exploratory research and analysis. Journal of computational chemistry. 2004;25(13):1605-12. Epub 2004/07/21. doi: 10.1002/jcc.20084. PubMed PMID: 15264254.

44. Kowieski TM, Lee S, Denu JM. Acetylation-dependent ADP-ribosylation by Trypanosoma brucei Sir2. The Journal of biological chemistry. 2008;283(9):5317-26. Epub 2008/01/01. doi: 10.1074/jbc.M707613200. PubMed PMID: 18165239.

45. Fahie K, Hu P, Swatkoski S, Cotter RJ, Zhang Y, Wolberger C. Side chain specificity of ADP-ribosylation by a sirtuin. The FEBS journal. 2009;276(23):7159-76. Epub 2009/11/10. doi: 10.1111/j.1742-4658.2009.07427.x. PubMed PMID: 19895577; PubMed Central PMCID: PMCPmc2805772.

46. Rardin MJ, Newman JC, Held JM, Cusack MP, Sorensen DJ, Li B, et al. Label-free quantitative proteomics of the lysine acetylome in mitochondria identifies substrates of SIRT3 in metabolic pathways. Proceedings of the National Academy of Sciences of the United States

of America. 2013;110(16):6601-6. Epub 2013/04/12. doi: 10.1073/pnas.1302961110. PubMed PMID: 23576753; PubMed Central PMCID: PMCPmc3631688.

47. Park J, Chen Y, Tishkoff DX, Peng C, Tan M, Dai L, et al. SIRT5-mediated lysine desuccinylation impacts diverse metabolic pathways. Molecular cell. 2013;50(6):919-30. Epub 2013/06/29. doi: 10.1016/j.molcel.2013.06.001. PubMed PMID: 23806337; PubMed Central PMCID: PMCPmc3769971.

48. Ogata N, Ueda K, Kagamiyama H, Hayaishi O. ADP-ribosylation of histone H1. Identification of glutamic acid residues 2, 14, and the COOH-terminal lysine residue as modification sites. The Journal of biological chemistry. 1980;255(16):7616-20. Epub 1980/08/25. PubMed PMID: 6772638.

49. Smith TJ, Schmidt T, Fang J, Wu J, Siuzdak G, Stanley CA. The structure of apo human glutamate dehydrogenase details subunit communication and allostery. Journal of molecular biology. 2002;318(3):765-77. Epub 2002/06/11. doi: 10.1016/s0022-2836(02)00161-4. PubMed PMID: 12054821.

50. Avalos JL, Boeke JD, Wolberger C. Structural basis for the mechanism and regulation of Sir2 enzymes. Molecular cell. 2004;13(5):639-48. Epub 2004/03/17. PubMed PMID: 15023335.

51. Avalos JL, Bever KM, Wolberger C. Mechanism of sirtuin inhibition by nicotinamide: altering the NAD(+) cosubstrate specificity of a Sir2 enzyme. Molecular cell. 2005;17(6):855-68. Epub 2005/03/23. doi: 10.1016/j.molcel.2005.02.022. PubMed PMID: 15780941.

52. Zhou Y, Zhang H, He B, Du J, Lin H, Cerione RA, et al. The bicyclic intermediate structure provides insights into the desuccinylation mechanism of human sirtuin 5 (SIRT5). The Journal of biological chemistry. 2012;287(34):28307-14. Epub 2012/07/07. doi: 10.1074/jbc.M112.384511. PubMed PMID: 22767592; PubMed Central PMCID: PMCPMC3436533.

53. Feldman JL, Dittenhafer-Reed KE, Kudo N, Thelen JN, Ito A, Yoshida M, et al. Kinetic and Structural Basis for Acyl-Group Selectivity and NAD(+) Dependence in Sirtuin-Catalyzed Deacylation. Biochemistry. 2015;54(19):3037-50. Epub 2015/04/22. doi: 10.1021/acs.biochem.5b00150. PubMed PMID: 25897714; PubMed Central PMCID: PMCPMC4470489.

54. Jeong SM, Xiao C, Finley LW, Lahusen T, Souza AL, Pierce K, et al. SIRT4 has tumor-suppressive activity and regulates the cellular metabolic response to DNA damage by inhibiting mitochondrial glutamine metabolism. Cancer cell. 2013;23(4):450-63. Epub

2013/04/09. doi: 10.1016/j.ccr.2013.02.024. PubMed PMID: 23562301; PubMed Central PMCID: PMCPmc3650305.

55. Komlos D, Mann KD, Zhuo Y, Ricupero CL, Hart RP, Liu AY, et al. Glutamate dehydrogenase 1 and SIRT4 regulate glial development. Glia. 2013;61(3):394-408. Epub 2013/01/03. doi: 10.1002/glia.22442. PubMed PMID: 23281078; PubMed Central PMCID: PMCPMC3552040.

56. Nakahara Y, Yamasaki M, Sawada G, Miyazaki Y, Makino T, Takahashi T, et al. Downregulation of SIRT4 Expression Is Associated with Poor Prognosis in Esophageal Squamous Cell Carcinoma. Oncology. 2016;90(6):347-55. Epub 2016/04/16. doi: 10.1159/000445323. PubMed PMID: 27082627.

57. Shi Q, Liu T, Zhang X, Geng J, He X, Nu M, et al. Decreased sirtuin 4 expression is associated with poor prognosis in patients with invasive breast cancer. Oncology letters. 2016;12(4):2606-12. Epub 2016/10/05. doi: 10.3892/ol.2016.5021. PubMed PMID: 27698834; PubMed Central PMCID: PMCPMC5038587.

58. Jayasena T, Poljak A, Braidy N, Zhong L, Rowlands B, Muenchhoff J, et al. Application of Targeted Mass Spectrometry for the Quantification of Sirtuins in the Central Nervous System. Scientific reports. 2016;6:35391. Epub 2016/10/21. doi: 10.1038/srep35391. PubMed PMID: 27762282; PubMed Central PMCID: PMCPMC5071856.

59. Braidy N, Poljak A, Grant R, Jayasena T, Mansour H, Chan-Ling T, et al. Differential expression of sirtuins in the aging rat brain. Frontiers in cellular neuroscience. 2015;9:167. Epub 2015/05/26. doi: 10.3389/fncel.2015.00167. PubMed PMID: 26005404; PubMed Central PMCID: PMCPMC4424846.

60. Baur JA, Pearson KJ, Price NL, Jamieson HA, Lerin C, Kalra A, et al. Resveratrol improves health and survival of mice on a high-calorie diet. Nature. 2006;444(7117):337-42. Epub 2006/11/07. doi: 10.1038/nature05354. PubMed PMID: 17086191.

61. Ajami M, Pazoki-Toroudi H, Amani H, Nabavi SF, Braidy N, Vacca RA, et al. Therapeutic role of sirtuins in neurodegenerative disease and their modulation by polyphenols. Neuroscience and biobehavioral reviews. 2017;73:39-47. Epub 2016/12/05. doi: 10.1016/j.neubiorev.2016.11.022. PubMed PMID: 27914941.

62. Gertz M, Nguyen GT, Fischer F, Suenkel B, Schlicker C, Franzel B, et al. A molecular mechanism for direct sirtuin activation by resveratrol. PloS one. 2012;7(11):e49761. Epub 2012/11/28. doi: 10.1371/journal.pone.0049761. PubMed PMID: 23185430; PubMed Central PMCID: PMCPmc3504108.

63. Diaz P, Phatak SS, Xu J, Astruc-Diaz F, Cavasotto CN, Naguib M.

6-Methoxy-N-alkyl isatin acylhydrazone derivatives as a novel series of potent selective cannabinoid receptor 2 inverse agonists: design, synthesis, and binding mode prediction. Journal of medicinal chemistry. 2009;52(2):433-44. Epub 2009/01/01. doi: 10.1021/jm801353p. PubMed PMID: 19115816.

64. Huang XP, Karpiak J, Kroeze WK, Zhu H, Chen X, Moy SS, et al. Allosteric ligands for the pharmacologically dark receptors GPR68 and GPR65. Nature. 2015;527(7579):477-83. Epub 2015/11/10. doi: 10.1038/nature15699. PubMed PMID: 26550826; PubMed Central PMCID: PMCPMC4796946.

Table 1. The identities and coverage of the human Sirt4 sequence to the template structures.

	Template protein (PDB ID)[a]	Identity	Coverage
Robetta Models	afSir2 (1S7G)	34%	90%
SWISS-MODEL1	zSirt5 (4UTN)	36%	82%
SWISS-MODEL2	hSirt5 (4G1C)	35%	82%
SWISS-MODEL3	hSirt5 (4G1C)	35%	82%

[a] The abbreviations are the same as those in the legend of Fig 1.

Table 2. A summary of the Ramachandran plots

	Model 1	Model 2	Model 3	Model 4	Model 5
SWISS-MODEL					
Favored	85.5%	83.8%	82.1%	-	-
Disallowed	1.3%	0.9%	1.3%	-	-
Robetta					
Favored	89.4%	88.9%	86.0%	84.7%	88.5%
Disallowed	0.0%	0.0%	0.0%	0.0%	0.9%
I-TASSER					
Favored	75.3%	69.8%	75.3%	70.2%	68.5%
Disallowed	2.1%	3.4%	2.1%	4.7%	5.5%

Table 3. A summary of the Verify3D results

	Model 1	Model 2	Model 3	Model 4	Model 5
SWISS-MODEL					
Quality [a]	Pass	Warning	Warning	-	-
% [b]	81.62	72.79	65.44	-	-
Robetta					
Quality [a]	Pass	Pass	Pass	Pass	Pass
% [b]	94.85	86.03	80.15	98.90	90.07

I-TASSER					
Quality [a]	Pass	Pass	Pass	Pass	Pass
% [b]	85.29	94.12	88.24	88.60	89.34

[a] The quality of the model structure as judged by Verify3D

[b] The percentage of the amino acid residues that scored ≥0.2 in the 3D/1D profile.

Table 4. A summary of the results from ERRAT

	Model 1	Model 2	Model 3	Model 4	Model 5
SWISS-MODEL					
Overall quality factor	69.318	67.424	73.864	-	-
Robetta					
Overall quality factor	93.939	82.955	91.667	94.318	93.561
I-TASSER					
Overall quality factor	98.462	99.231	98.438	92.015	99.615

Table 5. Energy calculations

	Model 1	Model 2	Model 3	Model 4	Model 5
SWISS-MODEL					
Rosetta [a]	2348.092	3385.999	1780.065	-	-
SPDBV [b]	-8092.796	-9112.978	-9764.719	-	-
Robetta					
Rosetta [a]	-250.860	-194.694	-176.061	-136.892	-196.233
SPDBV [b]	-14517.061	-14334.614	-14792.727	-14468.494	-14835.143
I-TASSER					
Rosetta [a]	1621.687	1372.388	1749.134	1447.029	1118.936
SPDBV [b]	-12257.712	-12059.712	-11537.371	-12181.420	-11788.820

[a] The energy score calculated by the Score algorithm of Rosetta.

[b] The energy calculated using Swiss PDB Viewer (kJ/mol).

Table 6. The evaluation of the Sirt4-NAD$^+$-GDH model

PROCHECK	
favored	83.0%
disallowed	0.0%
Verify3D	94.04% [a] (Pass [b])
ERRAT	90.034
Energy	
Rosetta [c]	-153.215
SPDBV [d]	-14365.062

[a] The percentage of amino acid residues that scored ≥ 0.2 in the 3D/1D profile.

[b] The quality of the model structure, as judged by Verify3D

[c] The energy score calculated using the Score algorithm of Rosetta.

[d] The energy calculated using Swiss PDB Viewer (kJ/mol).

Table 7. Distances (Å) between NAD^+ and the hydrogen bond-forming residues before and after the MD simulation

timing	E68	Q143	N144	D146	S262	N286	G288
0 ns	6.54	2.98	4.55	3.31	3.00	2.81	4.14
50 ns	3.45	3.05	2.76	2.93	2.64	2.94	2.96

Table 8. The free energy change associated with NAD^+ binding to the Sirt4 model and its energy components in kcal/mol

Energetics	Values
ΔE_{vdw}	-75.2 ± 0.5
ΔE_{elec}	-280 ± 2
ΔE^{MM}	-355 ± 2
$T\Delta S^{MM}$	-81.3255
ΔG^{MM}	-274
$\Delta G^{solv}{}_{polar}$	279 ± 2
$\Delta G^{solv}{}_{nonpolar}$	-9.03 ± 0.02
ΔG^{solv}	270 ± 2
ΔG_{bind}	-4